Determination of porosity in anisotropic fractal systems by neutron scattering

Xin Gu[a]* and David F. R. Mildner[b]

[a]Department of Geosciences, Pennsylvania State University, University Park, PA 16802, USA, and [b]NIST Center for Neutron Research, National Institute of Standards and Technology, Gaithersburg, MD 20899, USA. *Correspondence e-mail: xug102@psu.edu
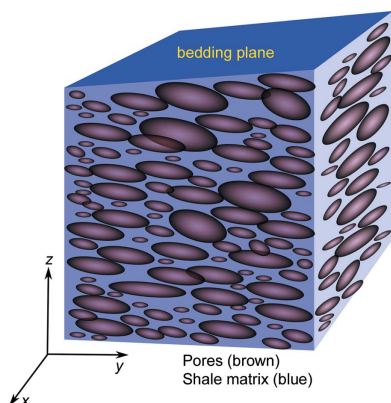
Small-angle scattering from two-phase isotropic systems requires the scattering to be invariant to determine the relative fractions of each phase in the material. For anisotropic systems the measurement yields a result that depends on the projection of the phases onto the scattering plane, normal to the incident radiation. When the scattering system has a unique axis such that there is no preferred direction in the plane normal to that axis, the scattering gives elliptical contours on the two-dimensional detector. Two different measurements of projected phases, one with the incident beam direction coincident with the unique axis and the other normal to that axis, can be combined to give a three-dimensional description of the system and therefore lead to a determination of the total porosity of the system.

1. Introduction

The use of small-angle neutron scattering (SANS) and ultra-small-angle neutron scattering (USANS) in geological research is increasing, particularly for shale rock [see reviews by Radlinski (2006) and Anovitz & Cole (2015)]. Neutron scattering techniques enable the investigation of pore-size distribution and pore connectivity from the nanometre to the micrometre scale, and these are crucial factors in characterizing hydrocarbon reservoirs and the hydrological properties of rock. Generally, neutrons are more penetrating than X-rays, giving neutrons the advantage of probing the bulk structure rather than the surface. Additionally, when neutrons are used, the scattering length density of the system can be changed by substituting deuterium for hydrogen, which provides information on the fluid accessibility of pores.

For rocks, a suitable fluid can be introduced into the pore system to change the scattering contrast between the otherwise empty pores and the mineral rock. This allows the scattering power of the connected (fluid-accessible) pores to be made the same as the average for the mineral, so that the observed scattered intensity is characteristic of the unconnected (fluid-inaccessible) pores. The porosities derived from neutron scattering should be comparable to those measured by other methods such as helium pycnometry, mercury porosimetry and nitrogen adsorption. However, the quantification of porosity in anisotropic geomaterials such as shale is still challenging, since most models for analyzing neutron scattering are based on the assumption of isotropy, *e.g.* the porosity features are orientation independent.

The preferred orientation in shale is attributed to the rearrangement of clay minerals during sedimentation and compaction that favor the orientation of platelets parallel to

bedding plane

z

y

x

Pores (brown)
Shale matrix (blue)

the bedding plane. Lacking any force to indicate otherwise, it is reasonable to assume that, on average, there is no preferred direction in the bedding plane (Fig. 1). Therefore, when the rock section is cut along the plane of bedding the scattering is azimuthally symmetric, with circular contours on the two-dimensional detector. When the rock section is cut in a plane that includes the normal to the bedding plane, the scattering is azimuthally asymmetric, with elliptical contours on the detector. This feature has been observed in different geomaterials like clay (Knudsen *et al.*, 2003; Méheust *et al.*, 2007; Hubert *et al.*, 2013), coal (Radlinski *et al.*, 2004), shale (Hall *et al.*, 1983; Anovitz & Cole, 2015; Gu *et al.*, 2015; Leu *et al.*, 2016) and slate (Hall & Mildner, 1983) by both small-angle neutron and X-ray scattering. However, only an empirical method of calculating porosity in anisotropic geomaterials has been reported (Gu *et al.*, 2015).

For an anisotropic system, Effler & Fellers (1992) developed a pseudo-invariant method to analyze fiber samples by considering the projection of the volume fraction of one of the phases onto a plane normal to the incident beam. They considered the directional dependence of the invariant for anisotropic samples and determined a parametric description of the degree of orientation. Pauw *et al.* (2010) and Li *et al.* (2014) also discussed the use of a pseudo-invariant to describe the pore structures in carbon fibers. The value of the pseudo-invariant in a particular direction (θ, φ) is given by $\int_0^\infty I(Q)_{\theta,\varphi} Q^2 \, dQ$, but this is not a true measure of the volume fraction of one of the phases. The value of the invariant varies as a function of the direction of the incident beam, and depends on the projected area of the scattering features onto the scattering plane for the measurement.

In our previous study, we presented a model to describe the azimuthal dependence of scattering from shale (Gu & Mildner, 2016). In this study, we investigate the anisotropy of

microstructure in shale through the analysis of scattering patterns taken at different incident directions to the beam and have determined the total porosity of shale by calculating the Porod invariant through the model. Though this work was motivated by geological research, this technique for calculating porosity from SANS asymmetric data can be applied more generally to any fractal sample that has a symmetric axis and shows elliptical contours on the plane normal to the symmetric axis.

2. Theoretical background

Summerfield & Mildner (1983) considered scattering from homogeneities that have rotational symmetry about a unique axis, such that the static pair correlation function, $g(\mathbf{r})$, is independent of the azimuthal angle with respect to the unique axis. They have shown that, in general, the scattering contours on a two-dimensional detector are elliptical of the form $(a^{-2}\cos^2\theta_0 + b^{-2}\sin^2\theta_0)$, where θ_0 is the angle that the scattering vector makes with the symmetry axis, and a and b are constants. More generally, the scattering plane may lie at some angle θ to the axis of symmetry such that the scattering vector $\mathbf{Q}$ has a polar angle θ_0 relative to the symmetry axis and an azimuthal angle φ within the plane given by $\cos\theta_0 = \cos\theta\cos\varphi$. This is depicted in Fig. 2. The scattered intensity as a function of azimuthal angle φ within the scattering plane becomes

$$I(Q) \simeq \left[\left(a^{-2}\cos^2\theta + b^{-2}\sin^2\theta \right) \cos^2\varphi + b^{-2}\sin^2\varphi \right]^{-1/2}, \quad (1)$$

where Q is the momentum transfer, defined as $Q = (4\pi/\lambda)\sin(\theta_s/2)$ with λ the wavelength of the incident radiation and θ_s the scattering angle. Two special cases exist: (i) when the scattering plane is normal to the axis of symmetry ($\theta = \pi/2$), $I(Q) \simeq b$, independent of azimuth (this is the case when the
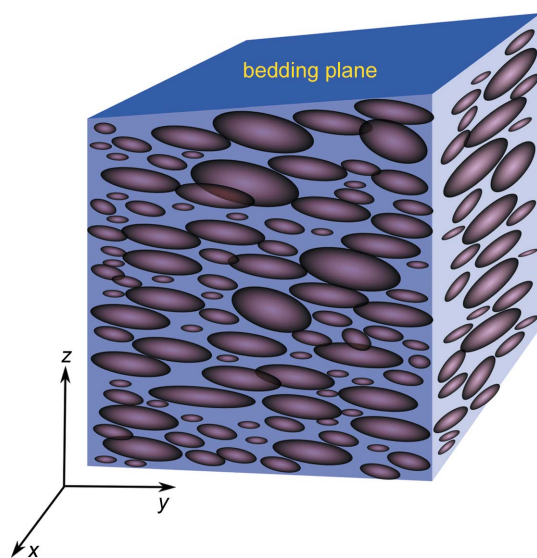

Figure 1
A schematic diagram depicting the pores (brown) in a shale mineral matrix (blue). The pores are flattened in the bedding plane (*XY* plane). Note that the sizes and numbers of pores are exaggerated.
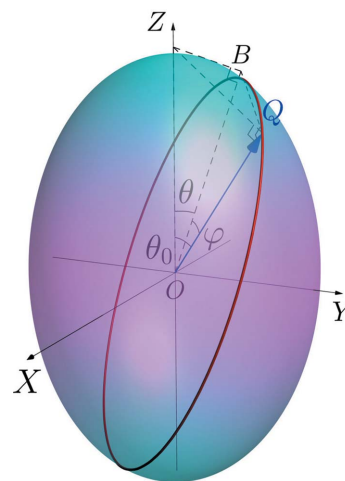

Figure 2
A schematic diagram depicting the surface of the prolate ellipsoid of revolution in reciprocal space, corresponding to a specific intensity marked as the red circle, lying at an angle θ to the scattering plane (*OBQ*). The polar angle θ_0 of the scattering vector $\mathbf{Q}(\theta, \varphi)$ relative to the axis of symmetry is given by $\cos\theta_0 = \cos\theta\cos\varphi$, where φ is the azimuthal angle relative to the projection (*OB*) of the symmetry axis in the scattering plane.

thin section is cut in a plane parallel to that of bedding); and (ii) when the scattering plane includes the axis of symmetry ($\theta = 0$), $I(Q) \simeq (a^{-2} \cos^2 \varphi + b^{-2} \sin^2 \varphi)^{-1/2}$ (this is the case when the thin section is cut in a plane perpendicular to that of bedding). Note that in this special case, the azimuthal angle $\varphi = \theta_0$, the polar angle of **Q** relative to the symmetry axis.

The scattering from geomaterials is often described as from a fractal system. That is, the intensity obeys a power law (over a limited range of scattering vector), such that $I(Q) = AQ^{-n}$, where A is a prefactor and n is the power law exponent. The azimuthal dependence of the scattered intensity from homogeneities with rotational symmetry may therefore be expressed by

$$I(Q, \varphi, \theta) = A_{\varphi,\theta}Q^{-n} = \left\{\left[\left(a^{-2} \cos^2 \theta + b^{-2} \sin^2 \theta\right) \cos^2 \varphi + b^{-2} \sin^2 \varphi\right]^{1/2} Q\right\}^{-n}. \quad (2)$$

The usual treatment of small-angle scattering from a two-phase isotropic incompressible system, such as particles suspended in a liquid or pores within a material, is to consider the scattering invariant, which is defined by a three-dimensional integral of the scattered intensity in reciprocal space (Porod, 1952),

$$V_{3d} = \int_0^\infty I(Q) \, d^3Q = 8\pi^3 (\Delta\rho)^2 \phi(1 - \phi), \quad (3)$$

or in spherical coordinates

$$V_{3d} = \int_0^\infty \int_0^\pi \int_0^{2\pi} I(Q, \varphi, \theta) \, Q^2 \, dQ \sin\theta \, d\theta \, d\varphi = 8\pi^3 (\Delta\rho)^2 \phi(1 - \phi). \quad (4)$$

Here, ϕ is the volume fraction of one phase (in our case pores) in a two-phase system, and $\Delta\rho$ is the contrast or the difference in the scattering length densities between the two phases.

For an isotropic medium, the intensity of the scattering at small angles is independent of the direction of the incident beam, such that the locus of the magnitude of the intensity as a function of **Q** in three-dimensional reciprocal space is the surface of a spheroid of radius Q. The intensity of the scattering is independent of angle so that the expression reduces to a one-dimensional integral over Q:

$$V_{1d} = \frac{V_{3d}}{4\pi} = \int_0^\infty I(Q)Q^2 \, dQ = 2\pi^2 (\Delta\rho)^2 \phi(1 - \phi). \quad (5)$$

For an anisotropic medium with an axis of symmetry that is in the scattering plane (e.g. a thin section cut normal to the bedding plane so that $\theta = 0$), the intensity of the scattering can be expressed as

$$I(Q, \varphi) = A_\varphi Q^{-n} = \left[\left(a^{-2} \cos^2 \varphi + b^{-2} \sin^2 \varphi\right)^{1/2} Q\right]^{-n}. \quad (6)$$

It is convenient to consider the case when a thin section is cut in a plane perpendicular to that of bedding and placed normal to the incident neutron beam, such that the scattering plane is that of the thin section. In this special case, the angle φ becomes the polar angle for the scattering vector **Q**, and the

scattering invariant becomes a two-dimensional integral over Q and φ:

$$V_{2d} = \frac{V_{3d}}{2\pi}$$
$$= \int_0^\infty \int_0^\pi \left(a^{-2} \cos^2 \varphi + b^{-2} \sin^2 \varphi\right)^{-n/2} Q^{2-n} \, dQ \sin\varphi \, d\varphi$$
$$= 4\pi^2 (\Delta\rho)^2 \phi(1 - \phi). \quad (7)$$

For the case of a powdered sample, we assume that the orientation of all grains is equiprobable. As an approximation, it is appropriate to consider the entire scattering averaged over all possible directions. We may, therefore, assume a constant prefactor so that the intensity may be expressed by $I_p = p^n Q^{-n}$. In this case, the intensity of the scattering is independent of orientation and the invariant may be written as a one-dimensional integral over Q as in equation (5):

$$V_{1d} = \frac{V_{3d}}{4\pi} = \int_0^\infty I_p Q^2 \, dQ = \int_0^\infty p^n Q^{2-n} \, dQ = 2\pi^2 (\Delta\rho)^2 \phi(1 - \phi). \quad (8)$$

Comparing the two expressions (7) and (8), we find

$$p^n = \frac{1}{2} \int_0^\pi \left(a^{-2} \cos^2 \varphi + b^{-2} \sin^2 \varphi\right)^{-n/2} \sin\varphi \, d\varphi$$
$$= \int_0^{\pi/2} \left(a^{-2} \cos^2 \varphi + b^{-2} \sin^2 \varphi\right)^{-n/2} \sin\varphi \, d\varphi$$
$$= b^n \int_0^{\pi/2} \left(1 - k^2 \cos^2 \varphi\right)^{-n/2} \sin\varphi \, d\varphi, \quad (9)$$

where $k = [1 - (b/a)^2]^{1/2}$ is the eccentricity of the ellipse.

Equation (9) has been solved numerically, and the results are shown in Fig. 3. When $n = 3$, equation (9) can be solved analytically, and we obtain

$$\frac{p}{b} = \left(\frac{a}{b}\right)^{1/3} = \left(1 - k^2\right)^{-1/6}. \quad (10)$$

Typically, geomaterials exhibit very rough surfaces and the fractal dimension is close to 3 (Radlinski, 2006). As a result, equation (10) may be a good approximation for p/b, and
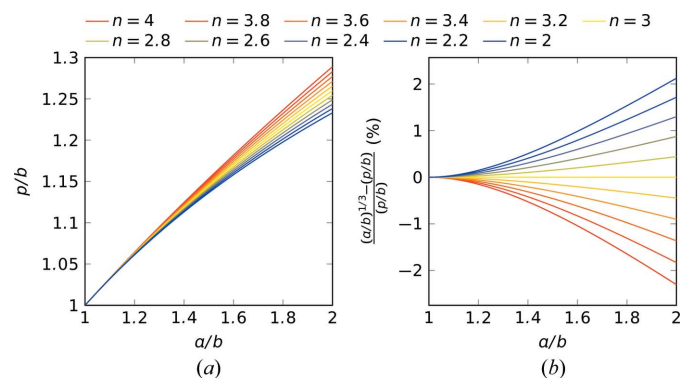

Figure 3
(a) p/b as a function of a/b for different values of the power-law exponent n, calculated by integrating equation (9) numerically. (b) The relative error in $(a/b)^{1/3}$ as a function of a/b and exponent n, where $(a/b)^{1/3}$ is the approximation of p/b given by equation (10).

analysis of powder measurements may provide a simple method of estimating the total porosity once a/b is obtained (details discussed below). When $2.6 < n < 3.4$ and $a/b < 2$, the relative error is smaller than 1%, as shown in Fig. 3.

3. Materials and experiment

The rock types used in this study are all Devonian-aged black shale and are from important gas-producing reservoirs in the Appalachian Basin, USA. They also represent different degrees of orientation due to variations in chemical composition and/or geological history. The key characteristics of these samples are summarized in Table 1. The average scattering length density (SLD) of the rock matrix is approximately 3.9×10^{10} cm^{-2} to 4.0×10^{10} cm^{-2}. The rock samples are considered as two-phase (pore–grain) systems, since the contrast of SLD between different minerals in black shale is much smaller than that with air or vacuum (Gu *et al.*, 2015).

Thin sections were prepared by cutting the rock both parallel and perpendicular to the bedding plane (referred to as rock thin sections). To obtain orientation-averaged samples, rock fragments were ground to particles with an agate mortar and pestle and dry sieved to 20–40 mesh (425–850 µm). For the sample collected from an outcrop of Marcellus shale (PLG), additional size fractions (mesh sizes 8–20, 40–60, 60–100 and 100–200, which represent 850–2360, 250–425, 150–250 and 75–150 µm, respectively) were prepared to test the potential effects of particle size on scattering. The particles were embedded in low-viscosity epoxy and cut to thin sections (referred to as epoxy thin sections). The thin sections were further polished to around 250 µm, and the actual thickness was measured by a digital micrometer with an uncertainty of 10 µm. To estimate the volume fraction of epoxy in the epoxy thin sections, scanning electron microscopy (SEM) imaging of the polished cross sections was performed using an environmental scanning electron microscope at the Materials Char-

Table 1
General characteristics for black shale samples selected for this study.

Total organic carbon (TOC) was determined by carbon combustion on acidified samples. Scattering length density (SLD) was calculated using the NIST neutron scattering calculator (https://www.ncnr.nist.gov/resources/activation) from the mineralogy as reported by Gu *et al.* (2016) and Gu & Mildner (2016).

Sample ID	Formation	Locality	Depth (m)	TOC (%)	SLD ($\times 10^{10}$ cm^{-2})
Erie	Dunkirk	Erie, PA	Outcrop, unweathered	8.3	3.9
SS8466	Marcellus	Snow Shoe, PA	2580	0.9	3.9
SS8721	Marcellus	Snow Shoe, PA	2658	5.2	4.0
PLG	Marcellus	Frankstown, PA	Outcrop, weathered	6.6	4.0

acterization Laboratory, Pennsylvania State University. Backscattered electron (BSE) images were obtained at 10 kV and a dwell time of 30 µs in low-vacuum mode. The grayscale BSE images were segmented manually in *ImageJ* to create a binary image of the mineral grain and epoxy (Abramoff *et al.*, 2004). The area fraction of the epoxy in the thin sections was determined using the particle analysis function in *ImageJ*. The averaged area fraction calculated from the binary images ($N > 10$) was assumed to be the same as the volume fraction probed by neutron scattering. The area fractions of epoxy in different samples are between 40 and 45% with uncertainties of around 3%.

The SANS and USANS measurements were performed on the NG3 (Glinka *et al.*, 1998) and BT5 (Barker *et al.*, 2005) instruments, respectively, at the National Institute of Standards and Technology (NIST) Center for Neutron Research (NCNR). SANS data were collected in three different configurations, with sample–detector distances of 1 and 4 m using 6 Å neutrons, and at 13 m with lenses. The latter configuration used MgF$_2$ lenses in order to extend the measurable range of the scattering vector, and a wavelength
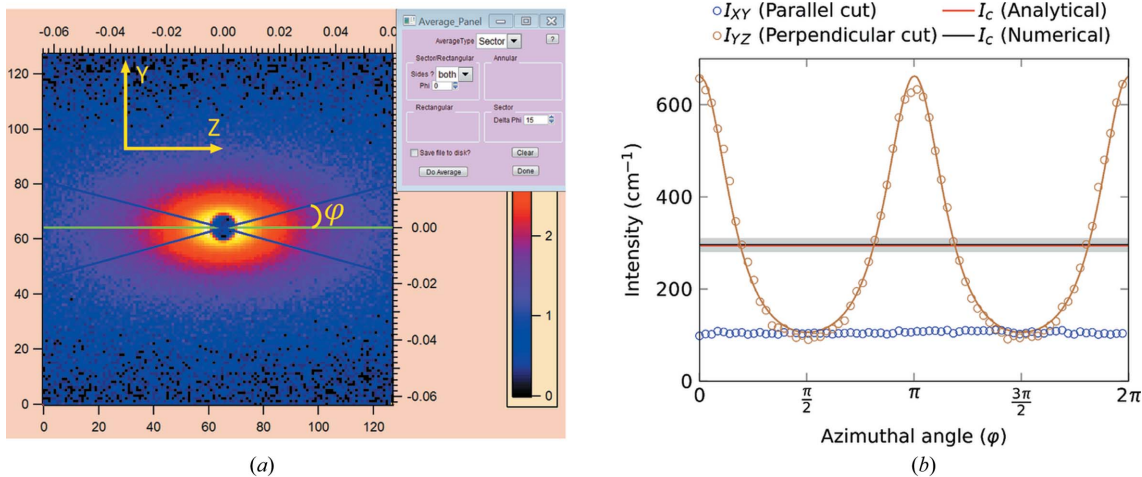

Figure 4
(*a*) Two-dimensional SANS spectra obtained for the Erie sample cut perpendicular to bedding (*YZ* plane) with a sample–detector distance of 4 m. (*b*) The anisotropic angular variation in the scattering intensity, I_{YZ} (perpendicular cut, in brown) and I_{XY} (parallel cut, in blue), with azimuthal angle (φ) at constant $Q = 0.01$ Å^{-1}. I_{YZ} was fitted to equation (6) (shown as a brown line). The azimuthal average of the intensity (I_C) in the *YZ* plane was obtained numerically from the *IGOR* package (black line) and obtained analytically from equation (15) (red line). These two lines are too close to be distinguished. The gray area shows two standard deviations of the numerical result.

$\lambda = 8.09$ Å to enable $Q = 1 \times 10^{-3}$ Å^{-1} to be reached for an overlap with the USANS range. Each sample was fixed onto a 1 mm thick quartz glass slide, which was itself attached to a gadolinium aperture of diameter 12.7 or 6.35 mm, depending on the size of the sample. Measurements on an azimuthally asymmetric sample taken on a conventional SANS instrument exhibit concentric intensity contours on a two-dimensional detector, as shown in Fig. 4(a).

The range of the scattering vector may be extended to lower values using a double-crystal diffractometer that records data in a horizontal scan and integrates the data in the vertical direction. USANS data were collected using a wavelength $\lambda = 2.38$ Å with $\Delta\lambda/\lambda = 5.9\%$. Scans were performed over the Q range $3 \times 10^{-5} < Q < 3 \times 10^{-3}$ Å^{-1} with a full width at half-maximum (FWHM) resolution of 2×10^{-5} Å^{-1} in the horizontal direction. The line average in the vertical direction (with an FWHM resolution of 0.117 Å^{-1}) requires that the USANS data, after background subtraction, be desmeared so that the data can be concatenated with the azimuthally averaged pinhole SANS data.

4. SANS data

After subtraction of background scattering from the empty quartz slide, the SANS data were normalized for detector sensitivity, sample transmission and thickness and scaled to yield absolute intensities (scattering cross section per unit volume) using the *IGOR* package developed at NCNR (Kline, 2006). The SANS from a thin section cut in a plane parallel to the bedding plane displayed symmetric contours on the two-dimensional detector so the data were circularly averaged to produce one-dimensional intensity, referred to as $I_X(Q)$. The SANS from a thin section cut in a plane perpendicular to the bedding plane (Fig. 4a) displays elliptical isointensity contours on the two-dimensional detector. Fig. 4(b) shows the contour at $Q = 0.01$ Å^{-1}, together with the fit to equation (6) with the best fitted value of $a/b = 1.72 \pm 0.12$ for the Erie sample.

The 30° sector averages about the shorter axis, corresponding to the direction in the bedding plane and labeled Y, and about the longer axis, normal to the bedding plane and labeled Z, are indicated by

$$I_Y(Q) = \langle I(0, Q \sin\varphi, Q \cos\varphi)\rangle_{-\pi/12 < \varphi + \pi/2 < \pi/12},$$
$$I_Z(Q) = \langle I(0, Q \sin\varphi, Q \cos\varphi)\rangle_{-\pi/12 < \varphi < \pi/12}, \quad (11)$$

where φ is the azimuthal angle defined relative to the normal direction. $I_Y(Q)$ and $I_Z(Q)$ represent two special cases of equation (6): $I_Z(Q) = I(Q, \varphi = 0) \cong a^n Q^{-n}$ and $I_Y(Q) = I(Q, \varphi = \pi/2) \cong b^n Q^{-n}$. The ratio $a/b = [I_Z(Q)/I_Y(Q)]^{1/n}$ can be obtained by fitting the data on a log–log plot over the scattering vector magnitude range $3 \times 10^{-3} < Q < 3 \times 10^{-2}$ Å^{-1}, with a power law exponent n. For this Q range the Erie sample has $a/b = 1.79 \pm 0.02$. As shown in Table 2, the prefactors for the X and Y orientations are very close for all four samples, indicating that both parallel and perpendicular cuts represent the same sample.

Table 2
Summary of the SANS measurements.

The scattering intensity was fitted to a simple power law, $I(Q) = AQ^{-n}$, over the scattering vector magnitude range $3 \times 10^{-3} < Q < 3 \times 10^{-2}$ Å^{-1}. The X orientation is for the sample cut parallel to bedding and exhibits circular contours. The Y, Z and C orientations are for the sample cut perpendicular to bedding and show elliptical contours (I_Y and I_Z are 30° sector averages of the short and long axes respectively, and I_c is the circular average from the *IGOR* package). The powder orientation is for the epoxy thin section of powder with a certain particle size (shown in parentheses) after subtraction of the epoxy scattering and has circular contours. The quoted uncertainty is one standard deviation from the mean.

Sample ID	Orientation	Thickness (μm)	n (average)	Prefactor A for average n ($\times 10^{-5}$ cm^{-1})
Erie	X	299		2.4 (0.1)
	Y	238		2.4 (0.1)
	Z	238	3.30	16.2 (0.4)
	C	238		7.4 (0.3)
	Powder (425–850 μm)	266		5.1 (0.3)
SS8466	X	366		4.0 (0.1)
	Y	297		3.8 (0.1)
	Z	297	3.07	13.9 (0.5)
	C	297		7.7 (0.3)
	Powder (425–850 μm)	293		6.1 (0.2)
SS8721	X	214		6.3 (0.1)
	Y	267		6.4 (0.2)
	Z	267	3.20	22.0 (0.5)
	C	267		12.8 (0.3)
	Powder (425–850 μm)	324		9.7 (0.2)
PLG	X	291		2.0 (0.1)
	Y	265		2.1 (0.1)
	Z	265		3.6 (0.1)
	C	265		2.7 (0.1)
	Powder (850–2360 μm)	289	3.41	2.4 (0.2)
	Powder (425–850 μm)	452		2.5 (0.2)
	Powder (250–425 μm)	321		2.5 (0.2)
	Powder (150–250 μm)	302		2.6 (0.2)
	Powder (75–150 μm)	292		2.6 (0.2)

Though the contours are elliptical, we can perform a full 2π azimuthal average of the intensity at a constant value of Q to obtain better statistics:

$$I_c(Q) = \langle I(0, Q \sin\varphi, Q \cos\varphi)\rangle_{0 < \varphi < 2\pi}$$
$$= \langle(a^{-2} \cos^2\varphi + b^{-2} \sin^2\varphi)^{-n/2}\rangle Q^{-n}. \quad (12)$$

If we assume $n = 3$, equation (12) becomes

$$I_c(Q) = \langle(a^{-2} \cos^2\varphi + b^{-2} \sin^2\varphi)^{-3/2}\rangle Q^{-3}$$
$$= (2b^3/\pi)Q^{-3} \int_0^{\pi/2} (1 - k^2 \cos^2\varphi)^{-3/2} \, d\varphi$$
$$= (2/\pi) b^3 (a/b)^2 \mathbf{E}(k) Q^{-3}, \quad (13)$$

where $\mathbf{E}(k)$ is the complete elliptical integral of the second kind. We generalize this form of the azimuthal average of the intensity for $n \neq 3$ by the expression

$$I_c(Q) = (2/\pi) b^n (a/b)^{n-1} \mathbf{E}(k) Q^{-n}. \quad (14)$$

Hence, we may state the azimuthally averaged intensity of the asymmetric scattering as $I_c(Q) \cong c^n Q^{-n}$, where

$$c^n = (2/\pi)\,\mathbf{E}(k)\,b^n(a/b)^{n-1} = (2/\pi)\,\mathbf{E}(k)\,b^n\big(1-k^2\big)^{(1-n)/2}. \tag{15}$$

The calculated I_c at $Q = 0.01$ Å^{-1} for the Erie sample is shown in Fig. 4(b), and the value is very close to the numerical output from *IGOR*. The c/b values calculated from a/b over the Q range $3 \times 10^{-3} < Q < 3 \times 10^{-2}$ Å^{-1} are in good agreement with the values from *IGOR* in all four samples (Table 3).

In a neutron scattering experiment, the measured scattering at high Q is from the incoherent scattering background (bkg). This incoherent scattering does not depend on Q and, though dependent on sample thickness, is identical for different measurements on the same sample (Fig. 5a). Thus, the entire scattering averaged over all possible directions (I_p) in the SANS range can be expressed as

$$\left.\begin{aligned} I_Z &= a^n Q^{-n} + \text{bkg} \\ I_Y &= b^n Q^{-n} + \text{bkg} \\ I_c &= c^n Q^{-n} + \text{bkg} \\ I_p &= p^n Q^{-n} + \text{bkg} \end{aligned}\right\} \Rightarrow I_p = I_c + \frac{p^n - c^n}{a^n - b^n}(I_Z - I_Y)$$

$$= I_c + \frac{(p/b)^n - (c/b)^n}{(a/b)^n - 1}(I_Z - I_Y). \tag{16}$$

We express I_c as a major component of I_p because of better statistics for circularly averaged intensity (I_c). a/b can be calculated from the $30°$ sector averages about the shorter and longer axes, as discussed above. p/b and c/b can be estimated from equations (10) and (15), respectively. If the scattering pattern is azimuthally symmetric as for the parallel-cut section, I_Y in equation (16) can be replaced with I_X.

Table 3
Comparison of the model with experimental results.

$a/b = [A(I_Z)/A(I_Y)]^{1/n}$, $c/b = [A(I_c)/A(I_Y)]^{1/n}$ (numerical) and $p/b = [A(I_p)/A(I_Y)]^{1/n}$ (powder) were calculated from the prefactors reported in Table 2. The modeled values of c/b and p/b were derived from equations (15) and (10), respectively.

Sample	a/b	c/b, numerical	c/b, model	p/b, powder	p/b, model
Erie	1.79 (0.02)	1.41 (0.02)	1.40 (0.01)	1.26 (0.02)	1.21 (0.01)
SS8466	1.52 (0.02)	1.25 (0.02)	1.25 (0.01)	1.16 (0.01)	1.15 (0.01)
SS8721	1.47 (0.02)	1.24 (0.02)	1.24 (0.01)	1.14 (0.01)	1.14 (0.01)
PLG	1.17 (0.01)	1.08 (0.01)	1.09 (0.01)	1.05 (0.01)	1.05 (0.01)

5. USANS data

A limitation of slit-smeared USANS measurements is that the data need to be converted into the SANS pinhole geometry. The desmearing algorithm (Lake, 1967) is only successful for azimuthally symmetric data, such as for samples cut parallel to the bedding plane, whereas samples cut at an angle to the bedding plane show asymmetric scattering. Gu & Mildner (2016) provide a method for converting asymmetric data obtained on a double-crystal diffractometer to a quasi-symmetric form, suitable for desmearing and concatenation with pinhole-geometry SANS data. The aspect ratio obtained from the elliptical contours of the SANS measurement is used to modify the slit-smeared USANS intensities such that the data are commensurate in the smeared and scan directions, producing quasi-symmetric contours.

When the perpendicular-cut sample is placed such that the axis of symmetry is in the scan direction (the Z measurement), the smeared intensities should be modified by a factor $(a/b)^{m/2}$, where m is the smeared USANS power-law exponent. Similarly, when the scan direction is within the bedding plane (the Y measurement), the smeared intensities should be modified
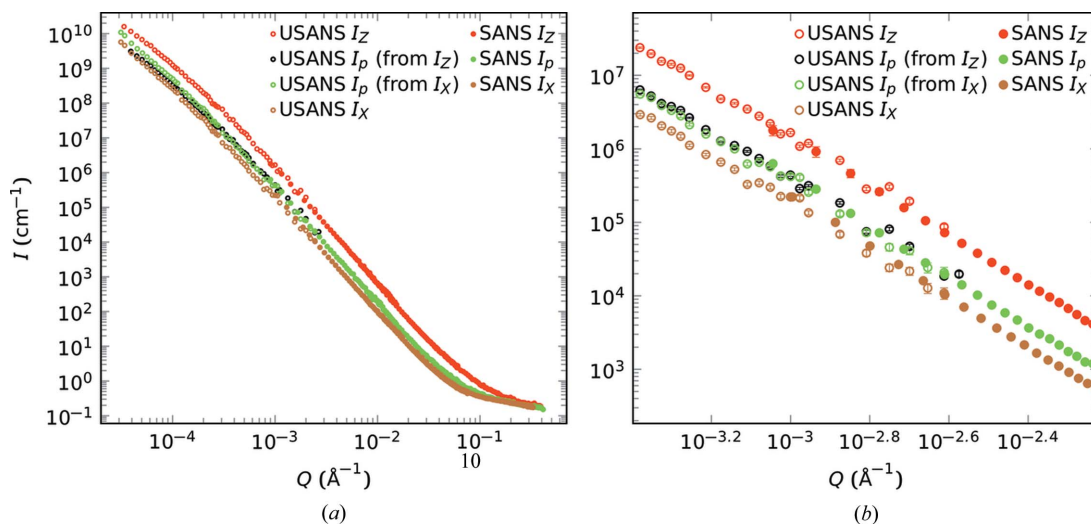

Figure 5
(a) Combined results from the desmeared USANS (open circles) and the SANS (solid dots) measurements for the Erie sample. (b) An enlarged view showing details of the overlapping region of the SANS/USANS transition. The USANS data for the X (I_X, in brown) and Z (I_Z, in red) orientations were measured on parallel- and perpendicular-cut samples, respectively, such that the latter is placed so that the scan direction is normal to the bedding plane ($\varphi = 0$). The intensities of the entire scattering averaged over all possible directions (I_p) in the USANS range are estimated from the USANS I_X (green) and I_Z (black) using equation (18) and (19), respectively. Both show smooth transitions with I_p in the SANS range (green), which were calculated using equation (16).

by a factor $(b/a)^{m/2}$. More generally, when the axis of symmetry is in the scattering plane and at an angle φ to the scan direction (see Fig. 6), the modification factor is given by

$$\frac{A_{\varphi\,\text{USANS mod}}}{A_{\varphi\,\text{USANS}}} = \left[\frac{\left(a^{-2}\cos^2\varphi + b^{-2}\sin^2\varphi\right)^{-1/2}}{(ab)^{1/2}}\right]^m$$
$$= \left[\frac{(1-k^2)^{1/2}}{1-k^2\cos^2\varphi}\right]^{m/2}. \quad (17)$$

Here, $A_{\varphi\,\text{USANS}}$ is the measured smeared USANS prefactor for a sample cut perpendicular to bedding and placed with the symmetry axis at an angle φ to the scan direction, and $A_{\varphi\,\text{USANS mod}}$ is the modified smeared USANS prefactor for the same measurement to correct for the asymmetry such that the data are quasi-symmetric. For the Z scan ($\varphi = 0$), this factor reduces to $(1-k^2)^{-m/4} = (a/b)^{m/2}$, and for the Y scan ($\varphi = \pi/2$), the factor reduces to $(1-k^2)^{m/4} = (b/a)^{m/2}$. However, a difficulty arises in the determination of the angle φ for the USANS measurement and this is addressed in Appendix A.

A simple method for calculating the entire scattering prefactor for USANS can be found from the modified prefactors for the perpendicular-cut sample, either within the bedding plane ($A_{Y\,\text{USANS mod}}$, $\varphi = \pi/2$) or its normal ($A_{Z\,\text{USANS mod}}$, $\varphi = 0$). That is, from equation (10) we have

$$\frac{A_{\text{p USANS mod}}}{A_{Y\,\text{USANS mod}}} = \frac{A_{\text{p SANS}}}{A_{Y\,\text{SANS}}} = \left(\frac{p}{b}\right)^n = \left(\frac{a}{b}\right)^{n/3} = \left(1-k^2\right)^{-n/6}, \quad (18)$$

where $A_{\text{p USANS mod}}$ is the modified USANS prefactor of the entire scattering averaged over all possible directions. Similarly,

$$\frac{A_{\text{p USANS mod}}}{A_{Z\,\text{USANS mod}}} = \frac{A_{\text{p SANS}}}{A_{Z\,\text{SANS}}} = \left(\frac{p}{a}\right)^n = \left(\frac{a}{b}\right)^{-2n/3} = \left(1-k^2\right)^{n/3}. \quad (19)$$

The parameter $A_{Y\,\text{USANS mod}}$ should be identical to the modified prefactor $A_{X\,\text{USANS mod}}$ for USANS measurement of a sample cut parallel to the bedding plane. The expression for the general angle φ is given in Appendix A. As shown in Fig. 5, all scattering intensities in the USANS range estimated from the parallel-cut measurements are identical to those estimated from the perpend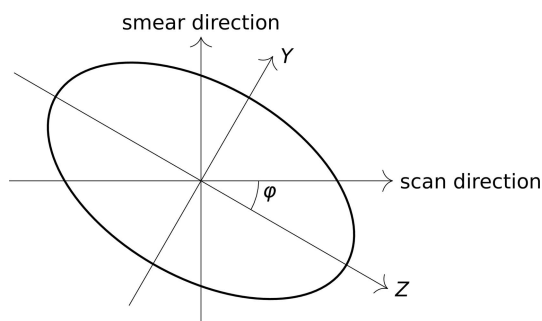icular-cut measurement, particularly for $Q >$ 10^{-4} Å^{-1}. Moreover, both parallel- and perpendicular-cut measurements show a smooth transition over all scattering intensities in the SANS range estimated through equation (16). It is noticeable that the consistency of I_p calculated from I_X and I_Z collapses at low Q ($Q < 10^{-4}$ Å^{-1}). There are several possible explanations for the inconsistencies:

(i) The scattering deviates from a simple power law at low Q. At low Q, a change in the slope of the scattering curve on a log scale exists in many geomaterials, showing a transition from mass fractal ($n < 3$) to surface fractal ($n > 3$) in the USANS range (Mildner & Hall, 1986; Allen, 1991; Radliński et al., 1999; Navarre-Sitchler et al., 2013; Bazilevskaya et al., 2015; Gu et al., 2015).

(ii) The degree of anisotropy determined by the aspect ratio a/b changes with Q.

(iii) The multiple scattering occurring with thick samples may result in artifacts of measurement at low Q, which is close to the incident beam. Therefore, if the information at low Q is important, it is recommended to take USANS measurements on thin sections cut both parallel and perpendicular to bedding (or at different azimuthal angles for the perpendicular cut) and average the I_p values calculated at different orientations.

6. Epoxy thin section

The scattering of shale powder (I_{powder}) in an epoxy thin section is calculated as

$$I_{\text{powder}} = \frac{I_{\text{section}} - \psi_{\text{epoxy}}I_{\text{epoxy}}}{\left(1 - \psi_{\text{epoxy}}\right)}, \quad (20)$$

where I_{section} is the scattering of the epoxy thin section, I_{epoxy} is the scattering of the epoxy itself and ψ_{epoxy} is the volume fraction of epoxy in the thin section, which is estimated through analysis of BSE images as discussed above. The powder was randomly impregnated in epoxy, with no apparent orientation under SEM. The SANS on all epoxy thin sections displayed symmetric contours on the two-dimensional
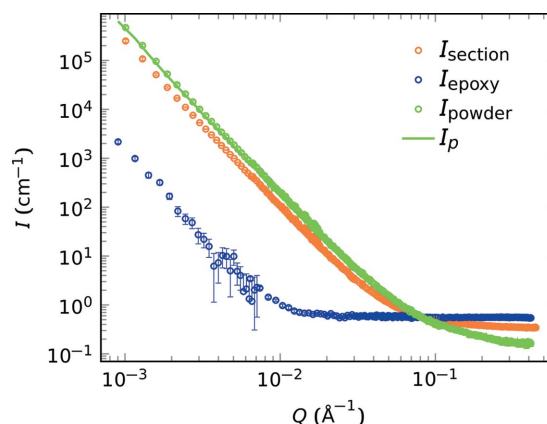

Figure 6
A schematic diagram showing an elliptical isointensity contour in the scattering plane. The z axis of symmetry is at an angle φ to the scan direction which has high resolution. The data are integrated along the smear direction, resulting in poor resolution.

Figure 7
The SANS results of epoxy thin sections of the Erie sample. I_{powder} was calculated from equation (20) and I_p was calculated using equation (16). Error bars are one standard deviation.

detector, so the data were circularly averaged to produce one-dimensional intensity as a function of the magnitude of Q. Fig. 7 shows that the scattering of the epoxy is relatively small (over two orders of magnitude lower than the shale) at low Q ($<10^{-2}$ Å^{-1}), but it introduces a high incoherent scattering background at high Q (probably due to the high hydrogen content of the epoxy). After subtraction of the scattering from the epoxy, the intensities of the scattering from the shale powder (I_{powder}, green circles in Fig. 7) of the Erie sample in the SANS region are almost identical to the entire scattering

averaged over all possible directions (I_{p}, green line in Fig. 7) calculated from equation (16).

We find that I_{powder} is close to I_{p} in the SANS range for all four samples, as shown in Table 3. This consistency is not surprising because the particles in the powder thin sections are randomly distributed; therefore, the orientation-dependent scattering intensities are physically averaged, a result similar to the numerically averaged scattering intensities (I_{p}). It is interesting that this consistency (the green dots I_{powder} and green line I_{p} in Fig. 8) breaks down for $Q < 10^{-4}$ Å^{-1}, for
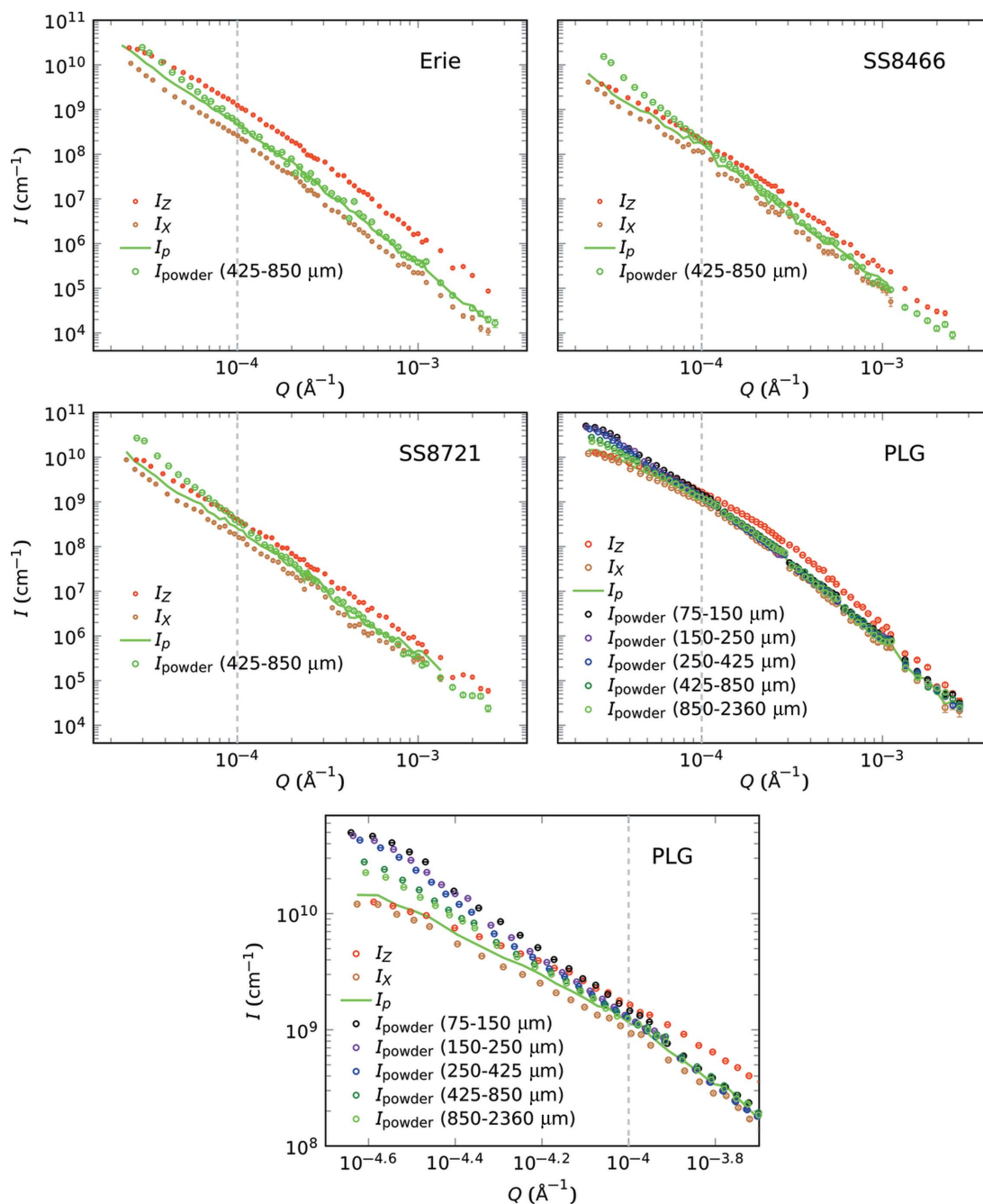

Figure 8
Data for four different rock samples, showing for each the desmeared USANS measurements for the parallel-cut sample (I_X, brown dots), the perpendicular-cut sample with the bedding plane normal to the scan direction of the instrument (I_Z, red dots) and the powder in an epoxy thin section (I_{powder}, green dots). The intensities of the entire scattering averaged over all possible directions (I_{p}) in the USANS range are estimated from the USANS I_X (green lines) measurement using equation (18). An enlarged view below shows details of the low-Q region for the PLG sample.

which I_{powder} is always higher than I_p for all four samples. It is likely that the scattering from grain–epoxy interfaces at $Q < 10^{-4}$ Å^{-1} contributes to the higher intensity of I_{powder}. It appears that this deviation increases with finer particles (Fig. 8, PLG sample), since the specific particle surface area (the particle–epoxy interface area per mass of sample) increases as the particle size decreases.

In all four samples of intact rock (thin sections), we observe a break in the gradient of the $\log I$ versus $\log Q$ plot, whereas this break is less observable for the powder samples. The transition from a surface fractal to a mass fractal occurs at a cut-off length that reflects the finite size of the system (Mildner & Hall, 1986). This cut-off length applies to fractal interfaces, indicating the maximum length of investigation that is sensitive to the interfacial structure of the microporous system. The microstructure of the intact rock is likely to be the same as that of the powder at small length scales (the high-Q region). However, the powders have more interfacial area at the larger length scales. Thus, the cut-off length is larger in powder samples than in intact rock, resulting in the change in gradient occurring at lower Q for the finer powder.

7. Summary

The scattering centers can only be observed projected on the scattering plane, which is fine for pores that are isotropic. In this study, we have outlined a schedule, suitable for anisotropic systems and summarized in Fig. 9, to generate an entire scattering intensity curve averaged over all possible directions, from which we may calculate the porosity of shale or anisotropic samples. We assume the following: (i) the scattering of the sample can be described as a power law over a wide range of scattering vector; (ii) a unique axis exists within the system; (iii) the aspect ratio does not change over a wide range of scattering vector; and (iv) the samples are homogeneous (cuts both parallel and perpendicular to bedding represent the same characteristics). With these assumptions, it is possible to generate the entire scattering curve through measurements on

Figure 9
The schedule for generating the entire scattering curve.

the cut that includes the unique axis (i.e. perpendicular to bedding) or on a randomly oriented sample (e.g. a powder).

We have shown that anisotropic features interrogated by small-angle scattering can best be observed when the unique direction is placed within the scattering plane. The scattered profile has concentric isointensity contours that are elliptical in shape, from which the aspect ratio a/b can be determined. This procedure, however, uses only a fraction of the data, and we suggest alternative methods that use the entire data set with better statistics available on the two-dimensional detector. If the sample is ground into a fine powder, we find that the azimuthally averaged data agree well with a model that assumes a value of a/b obtained from the SANS asymmetric data and a power-law exponent n close to 3. Furthermore, we have established a relationship between circular averaging of the asymmetric data and the ratio a/b obtained from sector averaging of the data.

Because the pore structure of shale is complex and the pore size covers a range from nanometres to micrometres (or even larger), in practice a combination of imaging (both in real space and in reciprocal space) and bulk tools (such as gas adsorption and liquid saturation/intrusion) are often used together to characterize multi-scale pore structure in shales (Anovitz & Cole, 2015; Leu et al., 2016). However, the pore characteristics measured through imaging of shale are typically orientation dependent, while those measured through bulk tools are orientation independent. The approach described in this paper makes it possible to derive volume-averaged orientation-independent porosity through neutron scattering measurement of thin sections of shale. This approach allows better characterization of the structure of the internal domains in porous media (Zachara et al., 2016).

This method has been applied to powder samples for which measurements have been analyzed in terms of fractal geometry. They show that the correlation length indicating the transition from a surface fractal to a mass fractal increases as the particle size becomes finer. At a result, the powder samples might not represent the inherent microstructure of intact shale at length scales larger than 1 μm ($Q < 10^{-4}$ Å^{-1}). Further research is needed to estimate and eventually eliminate the potential artifacts of pore characteristics through measurements of powder samples.

The approach outlined here might be useful for the analysis of relatively simple anisotropic systems that have symmetry around some unique axis. The example given is that of sedimentary rock, for which the axis is normal to the bedding plane. Such application might be found in metallurgy, where the axis is normal to the metal rolling plane, and in plastic fibers or superconducting wires, where the extrusion direction defines the axis.

APPENDIX A
Sample mounted at an orientation angle φ

Pinhole SANS is performed with a two-dimensional detector, so that regardless of the direction of mounting of the perpendicular-cut sample, the long and short axes can be
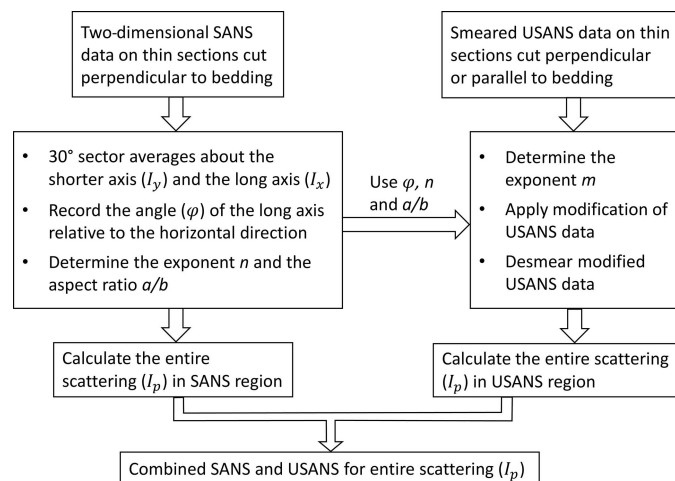
easily identified, from which the ratio a/b can be determined and equation (16) applied. For the slit-smeared USANS geometry, the measurement depends on the angle φ between the direction of the symmetry axis and the direction of the scan (see Fig. 6).

We assume that the sample remains mounted on the same gadolinium aperture and at the same orientation for each measurement, so that the angle φ can be determined from the SANS result. The ratio of modified prefactors for the general orientation angle φ relative to that for the Y measurement ($\varphi = \pi/2$) is given by

$$\frac{A_{\varphi\,\mathrm{USANS\,mod}}}{A_{Y\,\mathrm{USANS\,mod}}} = \frac{A_{\varphi\,\mathrm{SANS}}}{A_{Y\,\mathrm{SANS}}} = \left[\frac{\left(a^{-2}\cos^2\varphi + b^{-2}\sin^2\varphi\right)^{-1/2}}{b} \right]^n$$
$$= \left(1 - k^2\cos^2\varphi\right)^{-n/2}. \quad (21)$$

Combining equations (17) and (18) with (21), we obtain

$$\frac{A_{\mathrm{p\,USANS\,mod}}}{A_{\varphi\,\mathrm{USANS}}} = \left(1 - k^2\right)^{(m/4)-(n/6)}\left(1 - k^2\cos^2\varphi\right)^{(n-m)/2}, \quad (22)$$

which is valid for any orientation angle φ. All that is required to obtain $A_{\mathrm{p\,USANS\,mod}}$, the modified USANS prefactor of the entire scattering averaged over all possible directions, is the unmodified prefactor $A_{\varphi\,\mathrm{USANS}}$ for a measurement taken at the angle φ.

APPENDIX B
Sample cut at an oblique angle θ

Usually, samples are cut along the bedding plane so that the measurement gives circular contours, or cut in a plane that includes the symmetry axis to give elliptical contours. Here, we consider the general case where the sample is cut at some arbitrary angle θ to the axis of symmetry, as shown in Fig. 2. When the thin sections are made, the angle θ should be recorded. The line of intersection of a plane with an ellipsoid is an ellipse. Equation (2) shows that the semi-axes are given by $a' = (a^{-2}\cos^2\theta + b^{-2}\sin^2\theta)^{-1/2}$ and b. The ratio of the prefactors for measurements in directions along the larger and smaller axes is given by $A_Z/A_Y = (a'/b)^n = (1 - k^2\cos^2\theta)^{-n/2}$.

References

Abramoff, M. D., Magalhaes, P. J. & Ram, S. J. (2004). *Biophotonics Int.* **11**, 36–42.

Allen, A. J. (1991). *J. Appl. Cryst.* **24**, 624–634.

Anovitz, L. M. & Cole, D. R. (2015). *Rev. Mineral. Geochem.* **80**, 61–164.

Barker, J. G., Glinka, C. J., Moyer, J. J., Kim, M. H., Drews, A. R. & Agamalian, M. (2005). *J. Appl. Cryst.* **38**, 1004–1011.

Bazilevskaya, E., Rother, G., Mildner, D. F. R., Pavich, M., Cole, D., Bhatt, M. P., Jin, L. X., Steefel, C. I. & Brantley, S. L. (2015). *Soil Sci. Soc. Am. J.* **79**, 55–73.

Effler, L. J. & Fellers, J. F. (1992). *J. Phys. D Appl. Phys.* **25**, 74–78.

Glinka, C. J., Barker, J. G., Hammouda, B., Krueger, S., Moyer, J. J. & Orts, W. J. (1998). *J. Appl. Cryst.* **31**, 430–445.

Gu, X., Cole, D. R., Rother, G., Mildner, D. F. R. & Brantley, S. L. (2015). *Energy Fuels*, **29**, 1295–1308.

Gu, X. & Mildner, D. F. R. (2016). *J. Appl. Cryst.* **49**, 934–943.

Gu, X., Mildner, D. F. R., Cole, D. R., Rother, G., Slingerland, R. & Brantley, S. L. (2016). *Energy Fuels*, **30**, 4438–4449.

Hall, P. L. & Mildner, D. F. R. (1983). *J. Appl. Phys.* **54**, 427–428.

Hall, P. L., Mildner, D. F. R. & Borst, R. L. (1983). *Appl. Phys. Lett.* **43**, 252–254.

Hubert, F., Bihannic, I., Prêt, D., Tertre, E., Nauleau, B., Pelletier, M., Demé, B. & Ferrage, E. (2013). *Clays Clay Miner.* **61**, 397–415.

Kline, S. R. (2006). *J. Appl. Cryst.* **39**, 895–900.

Knudsen, K. D., Fossum, J. O., Helgesen, G. & Bergaplass, V. (2003). *J. Appl. Cryst.* **36**, 587–591.

Lake, J. A. (1967). *Acta Cryst.* **23**, 191–194.

Leu, L., Georgiadis, A., Blunt, M. J., Busch, A., Bertier, P., Schweinar, K., Liebi, M., Menzel, A. & Ott, H. (2016). *Energy Fuels*, **30**, 10282–10297.

Li, D., Lu, C., Wu, G., Hao, J., Yang, Y., Feng, Z., Li, X., An, F. & Zhang, B. (2014). *J. Appl. Cryst.* **47**, 1809–1818.

Méheust, Y., Dagois-Bohy, S., Knudsen, K. D. & Fossum, J. O. (2007). *J. Appl. Cryst.* **40**, s286–s291.

Mildner, D. F. R. & Hall, P. L. (1986). *J. Phys. D Appl. Phys.* **19**, 1535–1545.

Navarre-Sitchler, A. K., Cole, D. R., Rother, G., Jin, L. X., Buss, H. L. & Brantley, S. L. (2013). *Geochim. Cosmochim. Acta*, **109**, 400–413.

Pauw, B. R., Vigild, M. E., Mortensen, K., Andreasen, J. W. & Klop, E. A. (2010). *J. Appl. Cryst.* **43**, 837–849.

Porod, G. (1952). *Kolloid Z.* **125**, 108–122.

Radlinski, A. P. (2006). *Rev. Mineral. Geochem.* **63**, 363–397.

Radlinski, A. P., Mastalerz, M., Hinde, A. L., Hainbuchner, A., Rauch, H., Baron, M., Lin, J. S., Fan, L. & Thiyagarajan, P. (2004). *Int. J. Coal Geol.* **59**, 245–271.

Radliński, A. P., Radlińska, E. Z., Agamalian, M., Wignall, G. D., Lindner, P. & Randl, O. G. (1999). *Phys. Rev. Lett.* **82**, 3078–3081.

Summerfield, G. C. & Mildner, D. F. R. (1983). *J. Appl. Cryst.* **16**, 384–389.

Zachara, J., Brantley, S., Chorover, J., Ewing, R., Kerisit, S., Liu, C. X., Perfect, E., Rother, G. & Stack, A. G. (2016). *Environ. Sci. Technol.* **50**, 2811–2829.